Acta Astronautica 216 (2024) 105–119

Contents lists available at ScienceDirect

Acta Astronautica

journal homepage: www.elsevier.com/locate/actaastro

Development and simulation of a 3D printed liquid oxygen/liquid natural gas aerospike

L. Fadigati [a], F. Rossi [b], N. Souhair [c], V. Ravaglioli [a], F. Ponti [a,*]

[a] Alma Propulsion Laboratory, Department of Industrial Engineering, University of Bologna, Via Fontanelle 40, Forlì, FC, 47121, Italy
[b] Pangea Aerospace, C. Roc Boronat, 117, 08018, Barcellona Spain
[c] LERMA Laboratory Aerospace and Automotive Engineering School, International University of Rabat Sala Al Jadida, Rabat, 11100, Morocco

ARTICLE INFO

Keywords:
Aerospace propulsion
Aerospike
Plug nozzles
Numerical simulations
Supersonic flows

ABSTRACT

One of the most difficult aspects to solve, in the development of an aerospike engine, is the cooling of the throat and base regions. This issue is addressed nowadays by relying on new capabilities offered by additive manufacturing techniques together with novel powder materials, that allow to design complex shapes while keeping the prototyping cost low. The following work shows the design and manufacturing process of DemoP1, an aerospike engine demonstrator developed by Pangea Aerospace, that applies the new capabilities offered by additive manufacturing. To validate the development, the engine has been tested at the P8.2 test stand of the Germany Space Agency (Deutsches Zentrum für Luft-und Raumfahrt, DLR) in Lampoldshausen. Finally, a numerical strategy has been implemented and validated to simulate the engine flowfield, therefore obtaining relevant information that would be impractical to measure during tests, such as the pressure distribution along the plug and in the plume and the estimation of the heat flux on the throat and spike walls to be used to guide and validate the design process.

1. Introduction

Currently, rocket engines use traditional bell-shaped nozzles, that have a fixed area ratio and can therefore work at maximum efficiency only at a given altitude, corresponding to their design Nozzle Pressure Ratio (NPR). When the working NPR is lower than the design one (overexpansion), the exhaust gas is recompressed by the higher ambient pressure, and can even separate from the nozzle wall, leading to overheating issues. At high working NPR (underexpansion), the exhaust gas still expands beyond the nozzle exit section. In both operating conditions, the bell nozzle loses performance, therefore operating suboptimally during most of the launcher flight. Many solutions have been proposed to overcome standard nozzles drawbacks [1,2], none of which proved to be suitable for flight operation.

Plug nozzles have been first researched in the 50s [3–5] as a mean to achieve higher performance over a larger altitude range. Unlike other concepts, these theoretically provide a continuous altitude adaptation because the flow is free to expand along the plug, as it is no longer confined by solid boundaries [6,7]. Therefore, at working NPR lower than the design one, the flow expands until reaching ambient pressure without flow separation or normal shockwave, while at higher working NPR, the absence of an external wall allows the flow to expand more, again reaching ambient pressure at the nozzle exit section. Despite the superior performance, plug nozzles are very hard to cool down because the overall surface of thermal exchange is higher than in traditional nozzles [7,8]. Moreover, the throat section, featuring the highest heat flux [7], is also the one with the highest surface, leading to high thermal stress. Finally, cooling the plug tip is also challenging because of the narrow space available to place cooling channels in that region [7]. The latter issue has been solved by introducing the aerospike geometry, which is essentially a plug nozzle where the plug is truncated. The reduction of the plug surface reduces the thrust produced along the spike, but at the same time results in a reduction in dimensions and weight, eventually leading to a net gain in the thrust-to-weight ratio of the engine [9,10]. Also, this performance loss is partially recovered by the thrust produced at the base region, where the plug is truncated. Therefore, for the same expansion ratio, an aerospike is less efficient than a bell nozzle at the design point, but its efficiency is retained also further away from this point. Despite promising theoretical results, the manufacturing effort together with adverse funding circumstances set an end to aerospike development programs.

* Corresponding author.
E-mail addresses: luca.fadigati2@unibo.it (L. Fadigati), federico.rossi@pangeaaerospace.com (F. Rossi), nabil.souhair2@unibo.it (N. Souhair), vittorio.ravaglioli2@unibo.it (V. Ravaglioli), fabrizio.ponti@unibo.it (F. Ponti).

https://doi.org/10.1016/j.actaastro.2023.12.037
Received 7 September 2023; Received in revised form 12 December 2023; Accepted 16 December 2023
Available online 23 December 2023

Nomenclature

a_1	= k-ω SST parameter [−]
C_p	= specific heat capacity at constant pressure [J/(kg K)]
$C_{p_{amb}}$	= specific heat capacity at constant pressure at ambient condition [J/(kg K)]
$C_{p_{th}}$	= specific heat capacity at constant pressure at throat section [J/(kg K)]
$c_{s_{amb}}$	= speed of sound at ambient condition [m/s]
$c_{s_{inlet}}$	= speed of sound at inlet [m/s]
C_v	= specific heat capacity at constant volume [J/(kg K)]
C_μ	= k-ω SST parameter [−]
Co_{max}	= maximum Courant number [−]
Δe_p	= non dimensional pressure error [−]
e	= specific internal energy [J/kg]
e_T	= percentage thrust difference [−]
F	= convective flux vector
f	= focal length [m]
$\mathscr{T}_{th}$	= theoretical thrust [N]
h_e	= nozzle exit height [m]
I_{sp}	= specific impulse [s]
k	= turbulence kinetic energy [m2/s2]
k_{init}	= initial turbulence kinetic energy [m2/s2]
$k_{o,f}$	= outlet and farfield turbulence kinetic energy [m2/s2]
L	= plug length [m]
$\mathscr{M}$	= molar mass [kg/mol]
$\mathscr{M}_{amb}$	= molar mass at ambient condition [kg/mol]
$\mathscr{M}_{th}$	= molar mass at throat section [kg/mol]
N_{cells}	= mesh cells number [−]
n_{ps}	= number of pressure sensors in experiments [−]
p	= pressure [Pa]
p_{0inlet}	= inlet total pressure [Pa]
p_{amb}	= ambient pressure [Pa]
p_{th}	= throat section pressure [Pa]
Pr	= Prandtl number [−]
Pr_{th}	= Prandtl number at throat section [−]
$\dot{q}$	= heat flux [W/m2]
$\overline{R}$	= specific gas constant [J/(kg K)]
R	= generic source term [−]
s'	= non-dimensional curvilinear coordinate along aerospike inner wall [−]
s'_{th}	= non-dimensional curvilinear coordinate at throat section [−]
S	= scalar measure of the strain rate tensor [s-1]
s	= coordinate along the plug [m]
S_{ij}	= ij component of the strain rate tensor [s-1]
T	= temperature [K]
t	= time [s]
T_{amb}	= ambient temperature [K]
T_{cc}	= combustion chamber temperature [K]
T_{inlet}	= inlet temperature [K]
$T_{o,f}$	= outlet and farfield temperature [K]
T_{th}	= throat section temperature [K]
U	= vector of conserved variables [−]
u	= flow velocity [m/s]
u_i	= i-th component of the velocity vector [m/s]
V	= diffusive flux vector [−]
x_i	= i-th Cartesian coordinate [m]
β_1	= k-ω SST parameter [−]
β_2	= k-ω SST parameter [−]
β^*	= k-ω SST parameter [−]
ϵ	= turbulence kinetic energy dissipation rate [m2/s3]
γ	= specific heat ratio [−]
γ_{amb}	= specific heat ratio at ambient conditions [−]
γ_{th}	= specific heat ratio at throat section [−]
μ	= dynamic viscosity [Pa s]
μ_{inlet}	= dynamic viscosity at inlet [Pa s]
μ_{th}	= dynamic viscosity at throat section [Pa s]
ω	= specific turbulence dissipation rate [s-1]
ω_{init}	= initial specific turbulence dissipation rate [s-1]
$\omega_{o,f}$	= outlet and farfield specific turbulence dissipation rate [s-1]
ρ	= density [kg/s]
ρ_{amb}	= ambient density [kg/s]
ρ_{inlet}	= density at inlet [kg/s]
$\sigma_{\omega 1}$	= k-ω SST parameter [−]
$\sigma_{\omega 2}$	= k-ω SST parameter [−]
σ_{k1}	= k-ω SST parameter [−]
σ_{k2}	= k-ω SST parameter [−]
τ	= viscous stress tensor [Pa]
ξ	= sum of specific internal and kinetic energies [J/kg]

Acronyms

BiCG	BiConjugate Gradient
BiCGStab	BiConjugate Gradient Stabilized
CAD	Computer Aided Design
CEA	Chemical Equilibrium with Applications
CNC	Computerized Numerical Control
DILU	Simplified Diagonal-based Incomplete LU preconditioner
DLR	Deutsches Zentrum für Luft-und Raumfahrt
DMLS	Direct Metal Laser Sintering
EBW	Electron Beam Welding
FVM	Finite Volume Method
HLLC	Harten, Lax, Van Leer, Contact
ISCRA	Information Services Computer Resource Area
LOX	Liquid OXygen
M-VLED	Multi-Volume Laser Energy Density
NASA	National Aeronautics and Space Administration
NPR	Nozzle Pressure Ratio
OpenFOAM	Open Source Field Operation and Manipulation
RANS	Reynolds Averaged Navier-Stokes
SST	Shear Stress Transport

Nowadays, additive manufacturing techniques sparked a new wave of developments around the world because the geometrical complexity of the engine can be addressed with economically-viable processes [11,12].

Few research groups are working on the aerospike technology. At the Beijing University of Aeronautics and Astronautics, an optimization method has been developed to design the aerospike contour in order to maximize the total impulse from sea level to the design altitude [13]. A thrust vectoring control system [14] and ceramic additive manufacturing [15] have been studied at Technische Universität of Dresden. The researchers at Chungnam National University are working on an aerospike-shaped nozzle for a solid rocket motor [16]. Next-Aero [17], in collaboration with Australian Monash University, has developed an aerospike demonstrator built with the selective laser melting technique [18]. Pangea Aerospace [12,19], in collaboration with the company Aenium [20], is designing a propulsion system based on a low-cost, additively manufactured, aerospike technology.

Simulating an aerospike is a really important task to drive the design process, providing estimation of parameters that would be difficult to measure before the manufacturing of the system, like for example the heat flux through the walls of the throat and of the spike, or the flow

Table 1
DemoP1 parameters.

Propellants	LOX/LNG
Cycle	pressure-fed
Nominal chamber pressure	45 bar
$\mathcal{F}_{th}$ (sea level)	20 kN
I_{sp}	268 s
Mixture mass ratio	2.8
Expansion ratio	5
Dimensions	240 mm × 240 mm x 260 mm

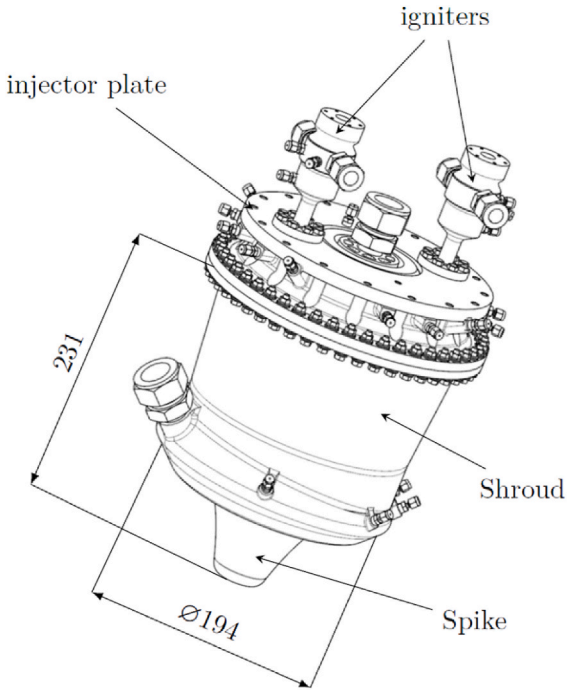

Fig. 1. DemoP1 drawing: the dimensions are in mm.

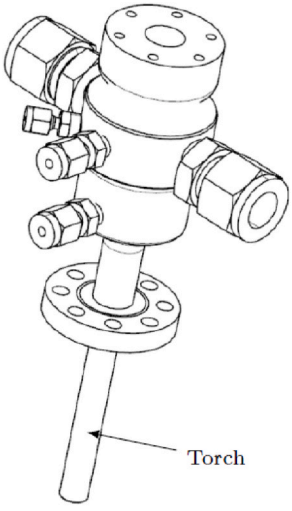

Fig. 2. Schematic drawing of the igniter.

characteristics around the spike, and the performance contribution of the base. Simulations are a real challenge because it is mandatory to consider also the interaction between the plume and the external flow in order to get accurate predictions. In Ref. [21] a linear plug nozzle has been simulated comparing the results with experimental pressure measurements along the plug and Schlieren photography of the plume. Similar validation has been performed in Ref. [22]. An aerospike with a rotating detonation chamber has been designed in Ref. [23] and then optimized using numerical simulations results and experiments [24] in order to maximize the produced thrust. Other important aspects of simulating a rocket engine is the combustion process modelling, as shown in Refs. [25–27].

The first part of this work summarizes the design and manufacturing process of DemoP1, an aerospike engine demonstrator developed by Pangea Aerospace [12]. The second part focuses on the development and validation of a numerical strategy targeted at the performance prediction and the flow and heat exchange characteristics of the aerospike engine.

2. DemoP1

DemoP1 is a technological demonstrator developed by Pangea Aerospace since the beginning of 2019 Q3. It is fed by Liquid OXygen (LOX) and Liquid Natural Gas (LNG) with an Oxidizer to Fuel (O/F) mass ratio of about 2.8. It has been designed to develop a thrust of 20 kN at sea level with a specific impulse of 268 s, a nominal combustion chamber pressure of 45 bar, and an expansion ratio of 5. The exit section diameter is 142 mm while the plug length is 75 mm. The throat section is radially located at 68 mm from the engine axis. In Table 1 the engine parameters are briefly summarized.

DemoP1 is composed of four main parts shown in Fig. 1: plug, shroud, injector plate, and igniters.

The spike contour has been designed relying on Angelino's method [3] and truncating the plug at 40 % of its length. This solution has been chosen to improve the cooling of the last portion of the plug and to fit the components inside the printer (an EOS M290 [28]) build plate. The reduction of the spike surface only implies a small performance reduction because the thrust is partially recovered by the base region contribution. The low expansion ratio yields an under-expanded plume at sea level, a peculiar choice for a rocket engine. This expansion ratio has been imposed to be able to fit the demonstrator inside the printer, neglecting performance requirements. This is mainly due to the fact that DemoP1 is targeted at demonstrating the feasibility of novel manufacturing techniques and the utilization of complex cooling systems involving both the fuel and oxidizer. Finally, DemoP1 aims at demonstrating the feasibility of LOX/LNG with aerospike engines.

2.1. Regenerative cooling system

Differently from the bell nozzle, in the aerospike, the throat section is located in the largest internal engine diameter making it more difficult to cool down since a high heat flux is distributed over a large region [7]. Both the plug and the external housing have to be cooled down but the amount of mass flow rate available is limited by the thrust requirement, therefore DemoP1 adopts a novel dual regenerative cooling system, in which the central plug is cooled by liquid oxygen while the external housing is cooled by LNG.

The coolant in the plug flows from the aerospike base to the combustion chamber in order to improve the cooling efficiency and to keep the coolant at a low temperature when it passes through the cooling channels at the throat section: the oxidizer enters in liquid state at the plug base, then it becomes transcritical at the throat section and finally becomes supercritical upon injection in the combustion chamber. The plug cooling channels have been designed with a spiral shape to retain a small cross-section, and therefore a high coolant velocity, where the engine section becomes the largest: at the throat. In this way, cooling efficiency is achieved only where it is more needed, thus minimizing pressure losses. The shroud cooling system is composed of axial channels fed by LNG flowing from the cowl lip to the injector head. Due to the additive manufacturing process used to build DemoP1, the internal roughness of the cooling channels is higher than in conventional milled ones. This involves higher turbulence and consequently a high heat

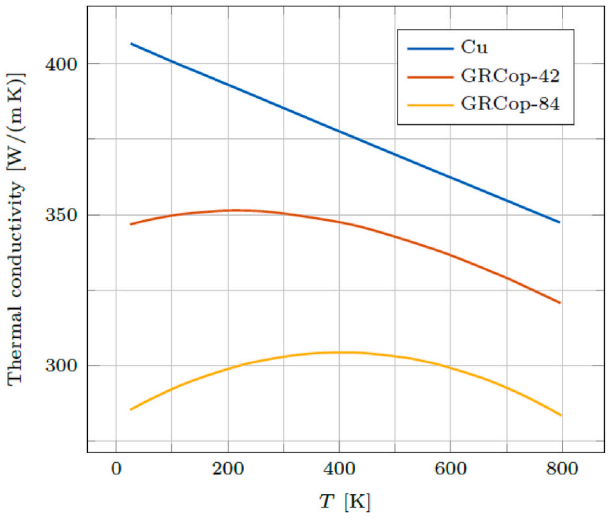

Fig. 3. Thermal conductivity of copper alloys.

Fig. 4. Printed shroud.

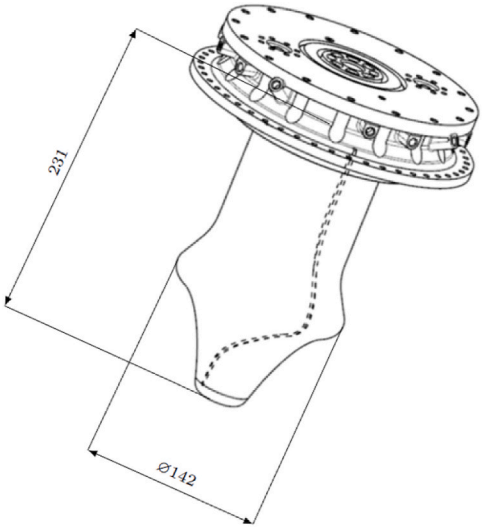

Fig. 5. Plug with the welded cover: the dimensions are in mm.

transfer. The fuel and the oxidizer gain enthalpy while cooling the engine walls and are injected into the combustion chamber in a supercritical, gas-like state. This improves mixing, therefore allowing to build a shorter chamber while still retaining the same combustion efficiency.

2.2. Ignition system

The ignition system uses gaseous oxygen and gaseous hydrogen. The igniters operate at a chamber pressure of 1 MPa and an O/F mass ratio of 40 inside the main chamber. At the end of the tube, the O/F ratio is reduced to 6 to obtain a high-temperature torch. The temperature of the igniter walls is kept low using a bypass system, therefore only part of the fuel is injected in the igniter combustion chamber leading to low combustion temperature. The majority of the fuel is deviated and meets the incoming combustion products at the exit section of the igniter, where main combustion is triggered with a flame temperature over 3000K. The igniters are additively manufactured using Inconel 718 [29] because it provides an excellent strength up to 1200K, allowing to avoid an active cooling system. Fig. 2 shows a CAD drawing of the igniter.

2.3. Interfaces

DemoP1 has two main propellant inlets for the liquid oxygen and the LNG. LOX enters through a downcomer that reaches the base of the plug, before entering the cooling channels, while the LNG line is connected through a radial boss on the shroud, just upstream of the cowl lip. Both interfaces are equipped with National Pipe Threads (NPT) and sealed with Polytetrafluoroethylene (PTFE) rated for cryogenic temperatures. The demonstrator is composed of only two parts, the plug and the shroud, that are assembled through the main engine bolted flange, below the injector head. The igniters are also mounted via sealed flanges on top of the injector head. All pressure and temperature sensors are connected via NPT and British Standard Pipe Threads (BSPT), while the accelerometers are installed on blind holes. Finally, the engine is interfaced to the thrust mount via a structural flange located above the injector head, and the thrust mount is fixed to the bench with 3 bolted connections.

2.4. Manufacturing process

DemoP1 has been additively manufactured using the EOS M 290 machine [28] which is a 3D printer based on the Direct Metal Laser Sintering (DMLS) technology. The combination of this technique with the Multi-Volume Laser Energy Density (M-VLED) [30] allows for building complex shapes and for dynamically controlling the laser energy density in order to tailor the local yield strength, elongation at break, thermal conductivity, hardness, surface roughness, and residual strength.

The structural material of the thrust chamber is GRCop-42, a copper alloy (Cu–Cr–Nb) developed by the National Aeronautics and Space Administration (NASA) for regeneratively-cooled combustion chambers and nozzles [31,32]. This material has been chosen for its high strength and high thermal conductivity, which are especially important to manage the thermal loads developed by an aerospike engine. Fig. 3 shows the thermal conductivity of GRCop-42 compared with other copper alloys and pure copper [33]. GRCop-42 features high thermal conductivity also at high temperatures, almost like pure copper, while its tensile strength is one order of magnitude higher. The material is also resistant to blanching and oxidation, which is especially important when using LOX as a coolant. The surface roughness level is very important, especially for the cooling channels, and has been deeply characterized. High roughness leads to a more efficient thermal exchange, but at the same time also to a higher pressure loss through the circuit. Therefore, the channels have to be carefully dimensioned to account for the high roughness environment generated by the manufacturing technique. Also, the part must be designed in order to be able to remove the powder

Fig. 6. Machined shroud liner.

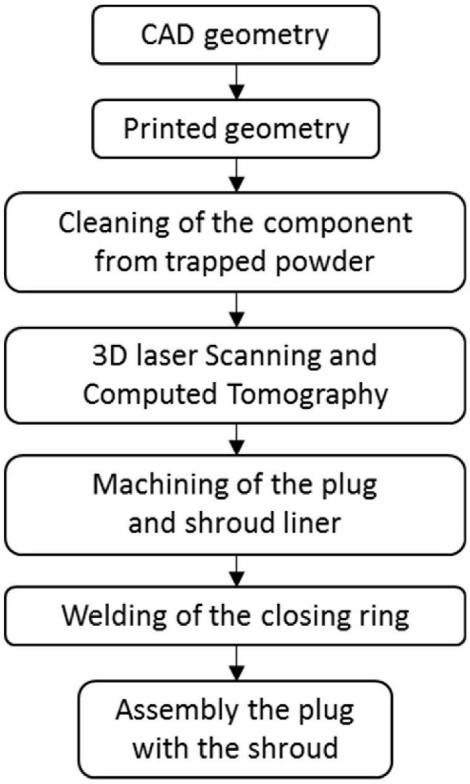

Fig. 7. Manufacturing process.

left after printing with a simple shaker and pressurized air. The cleaning process is very important because if the internal cavities are not perfectly cleared, the following heat treatments would sinter the residual powder, generating a partial or complete obstruction of the channels, leading to an unusable engine.

2.4.1. Shroud

Fig. 4 shows the printed shroud. It contains many small axial channels to cool down its internal wall. To remove the unused powder that fills these channels, a dedicated system of ports and ducts has been designed. The powder is removed by gravity, compressed air, and by a mechanical action, taking care of not providing any damage to the component. This process has been repeated many times in combination with inspection of all channels by means of a micro-fibrescope: due to the size and shape of the channels, this is the only way to check their clearance.

2.4.2. Plug

The plug is the most complex part of the engine (Fig. 5), as it is built in one piece together with the injector head. The latter features small manifolds and hundreds of injector elements, leading to a complex and packed internal geometry that hinders powder removal. To ease the process, the injector head has been printed with a circular opening to easily remove the powder, which is then closed by a welded ring.

After the cleaning process, despite the high thermal conductivity and high strength of GRCop-42, additional heat treatment has been necessary to improve these two properties. The plug and the shroud have been heat treated while still attached to the build plate to heal and release residual stresses.

2.4.3. Liner machining

The liner inside the combustion chamber is fundamental to exchange heat with the coolant fluid, therefore its actual thickness has to be carefully dimensioned. The only way to ensure the required level of accuracy is by machining since the additive manufacturing process cannot achieve this high precision. In addition, the subsequent heat treatment slightly modifies the final dimensions.

The cooling channels are inaccessible, therefore direct measurements are not possible. Hence, 3D laser Scanning and Computed Tomography have been used to determine the actual liner thickness. These two methods allow to obtain the liner size and to calculate a path for the CNC machine.

The chips and burrs produced by machining have been removed by high-pressure air and ultrasonic cleaning. Fig. 6 shows the shroud liner after machining.

2.4.4. Injector head

The injector head has been additively manufactured in one piece with the plug. The powder removal opening has been closed using Electron Beam Welding (EBW) [34]. This welding technique has been selected due to its high-power density and small heat-affected zones, that guarantee high-quality welded joints. Nevertheless, EBW is a very expensive process and it can be used in a very limited range of thicknesses. The absence of filler metal implies that the edges of the two components must be in contact without any separation. Welding is performed in vacuum condition, therefore no additional gas is required to protect the components from oxidation. After welding, the component has been pressurized at 1.2 times the nominal pressure to detect any possible leaks and verify the structural integrity of the joint.

2.4.5. Assembly

The plug and injector head are assembled with the shroud by means of the bolted flange shown in Fig. 1. RACO® spring-energized polymer seals [35] have been selected instead of metal o-rings, due to the low strength and hardness of the GRCop-42 alloy.

2.4.6. Summary of the manufacturing process

Fig. 7 sums up the manufacturing process described before. First, the geometry is drawn in a Computer-Aided Design (CAD) software, then it is printed with the DMLS method. The parts are cleaned from the trapped powder. Then, the plug and the shroud are inspected with 3D laser Scanning and Computed Tomography generating the surfaces of actual component in order to obtain a path for the CNC machine and to correct the liner thickness. Finally, the closing ring is welded in place and the plug is assembled with the shroud.

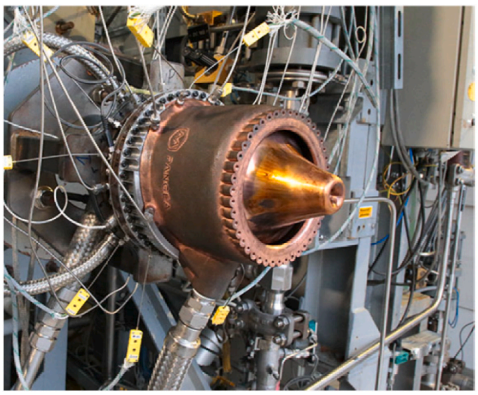

Fig. 8. Experimental test setup.

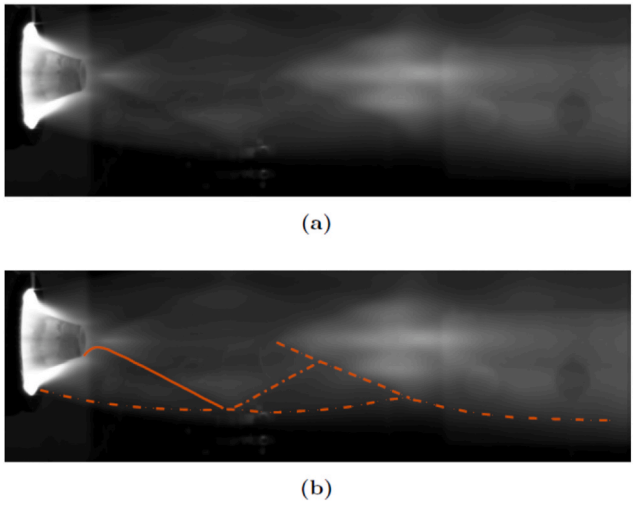

Fig. 9. High-speed camera averaged image: trailing shock (solid line), trailing shock reflection (dash-dotted line), shear layer (loosely dashed line), shock wave (dashed line).

3. Experimental tests

DemoP1 has been tested at the P8.2 stand [36,37] of the Germany Space Agency (DLR) in order to prove that it is capable of operating in nominal working conditions for a time interval similar to the burning time of a launcher's first stage. Furthermore, the ignition system and the cooling system have been tested to verify their capability to start combustion and cool the engine wall. Finally, the last aim of the test was to verify the reusability of the engine. Fig. 8 shows the experimental setup. The engine inlet is connected with flexible hoses in order to compensate for eventual thermal expansion and contraction. The demonstrator has been sealed with a stainless-steel cap and then pressurized with helium at 5 bar to check for any leakage. The first test consists of cold-flow checks to measure the pressure drop along the cooling lines and determine the priming time of the engine cavities in order to accurately time the startup procedure. The hot-fire tests allow to characterize the startup, shutdown, and steady-state behaviors.

The facility has been equipped with a high-speed camera, Photron Mini UX100, model 800k-*M*-1 [38] equipped with AF-S Nikkor $f = 50$ mm lens, capable of recording 8000 frames per second with a resolution of 1280 × 392 pixels. Two Wika Model A-10 pressure sensors [39] are connected through a cooling coil to the injector head, to measure the combustion chamber pressure. The coils are long enough to avoid that the hot gases reach the sensors. This solution does not allow capturing high-frequency pressure variations, but it is suitable to measure the steady state total pressure in the combustion chamber. These two sensors have a measurement accuracy lower than 0.06 bar.

The test considered in this paper is that in which DemoP1 works in a steady state condition with a combustion chamber total pressure set to 40.5 bar: 90 % of the design combustion chamber total pressure. The images captured by the high-speed camera have been aggregated to obtain the averaged position of the flow features. Fig. 9a shows the result of this image post-processing. No data can be obtained from the region close to the spike because the image exposure is too high. Nevertheless, the trailing shock (solid orange line in Fig. 9b) and its reflection on the shear layer (dash-dotted orange line in Fig. 9b) are visible. From this image, it is possible to extract also the flow shear layer (loosely dashed orange line in Fig. 9b) and the shock which delimits a high-temperature region (dashed orange line in Fig. 9b). These extracted features are compared to the simulations results in Section 6.2.

4. Numerical methodology

In this section, a numerical strategy to simulate the engine described in Section 2 is shown. It is based on the Favre averaged Navier-Stokes [40] equations completed with the *k*-ω SST model. The equations have been discretized and solved using *dbnsTurbFoam*, a solver included in *foam-extend* [41]. Harten–Lax–van Leer Contact (HLLC) [42] is the numerical scheme chosen to evaluate the fluxes between the mesh cells. The flow thermodynamic properties have been obtained using Chemical Equilibrium Applications (CEA), a code developed by NASA to calculate the equilibrium chemical composition of reacting substances [43]. This methodology is validated in Section 5 using the experimental data shown in Ref. [44] and then it has been used to simulate DemoP1 in Section 6.

4.1. Governing equations

The governing equations consist in the conservation of mass, momentum, and energy; respectively Equations (1)–(3).

$$\frac{\partial \rho}{\partial t} + \nabla \bullet (\rho \mathbf{u}) = 0 \tag{1}$$

$$\frac{\partial (\rho \mathbf{u})}{\partial t} + \nabla \bullet (\rho \mathbf{u} \bigotimes \mathbf{u}) = -\nabla p + \nabla \bullet \tau \tag{2}$$

$$\frac{\partial (\rho \xi)}{\partial t} + \nabla \bullet [(\rho \xi + p)\mathbf{u}] = \nabla \bullet (\tau \bullet \mathbf{u}) + \nabla \bullet \dot{\mathbf{q}} \tag{3}$$

In the previous equations ρ is the flow density, $\mathbf{u}$ is the flow velocity, p is the flow pressure, τ is the flow stresses, $\dot{\mathbf{q}}$ is the heat flux and ξ is the sum of the specific internal energy e, which is function of p and T and the specific kinetic energy defined as $\frac{1}{2}\mathbf{u} \bullet \mathbf{u}$.

According to Ref. [6], the frozen equilibrium hypothesis leads to underestimate the performance, typically by 1–4 %, but as shown in Ref. [45], due to the low length of the engine, the high flow velocity, and supposing a complete chemical equilibrium inside the combustion chamber, the chemical reactions have no time to take place close to the engine. Therefore, a frozen flow composition will be considered an acceptable hypothesis in the simulation domain. More details about the flow properties will be provided in Section 3.2. The flow has been assumed to behave as a perfect gas, while the Stokes' hypothesis [46] and the Fourier law [47] are used to evaluate the heat due to conduction.

Navier-Stokes equations have been averaged according to the Favre averaging procedure [40], while turbulence has been modelled with a two-equations RANS model in order to obtain acceptable results while limiting the computational burden. Between the ones proposed in the literature, *k*-ω SST (Shear Stress Transport), developed by Menter [48], has been chosen because it overcomes the drawback of *k*-ϵ method, developed by B. Launder and D. Spalding [49], and *k*-ω method, developed by Wilcox [50–53], combining their advantages. Therefore,

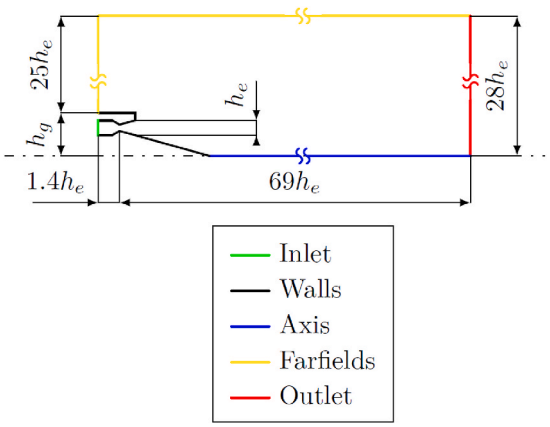

Fig. 10. Simulation domain and boundaries.

this model behaves like k-ϵ far away from walls and like k-ω close to them, and it can be used in flows with a strong adverse pressure gradient, while it is able to capture the boundary layer separation. Thanks to the previously mentioned advantages, k-ω SST has been used in other simulations [23,54,55], leading to acceptable results. This choice leads to the following additional equations for the model:

$$\frac{\partial(\rho k)}{\partial t}+\nabla\bullet(\rho k u)=P-\beta^{*}\rho\omega k+\frac{\partial}{\partial x_j}\left[(u+\sigma_k\mu_t)\frac{\partial k}{\partial x_j}\right] \tag{5}$$

$$\frac{\partial(\rho\omega)}{\partial t}+\nabla\bullet(\rho\omega u)=\frac{\gamma}{v_t}P-\beta_1\rho\omega^2+\frac{\partial}{\partial x_j}\left[(\mu+\sigma_\omega\mu_t)\frac{\partial\omega}{\partial x_j}\right] + 2\rho(1-F_1)\sigma_{\omega 2}\frac{1}{\omega}\frac{\partial k}{\partial x_j}\frac{\partial\omega}{\partial x_j} \tag{6}$$

P is the turbulent kinetic energy production term and the turbulent viscosity model adopted is the one shown in Ref. [56]:

$$P=\sum_{i,j}\tau_{ij}\frac{\partial u_i}{\partial x_j} \tag{7}$$

$$v_t=a_1\frac{k}{max(a_1\omega,\ F_2S)} \tag{8}$$

In Equation (8), S is a scalar measure of the strain rate tensor: $S=\sqrt{2S_{ij}S_{ij}}$ and $S_{ij}=\frac{1}{2}\left(\frac{\partial u_i}{\partial x_j}+\frac{\partial u_j}{\partial x_i}\right)$. Constants σ_k, σ_ω, β, γ have been obtained using the following relationship:

$$\varphi=F_1\varphi_1+(1-F_1)\varphi_2 \tag{9}$$

Where φ is a generic constant and F_1 is the blending function which is 1 near the surface and 0 faraway from walls. In all the simulations performed in this work, the values of the k-ω SST coefficients have been chosen according to Ref. [56]: $\sigma_{k1}=0.85$, $\sigma_{k2}=1.0$, $\sigma_{\omega1}=0.5$, $\sigma_{\omega2}=0.856$, $\gamma_1=0.5532$, $\gamma_2=0.4403$, $\beta_1=0.0750$, $\beta_2=0.0828$, $\beta^*=0.09$, $\alpha_1=0.31$. β^* has been introduced in Ref. [50] and is related to k, ϵ, and ω through the expression $\omega=\frac{\epsilon}{\beta^* k}$.

4.2. Chemistry model

As mentioned in Section 3.1, the flow composition has been assumed to be frozen. Its thermodynamic properties have been evaluated using the CEA (Chemical Equilibrium with Applications) software [57,58], a code developed by NASA to calculate the composition of reacting substances when they reach the equilibrium condition. This algorithm is based on the minimization of Gibbs free energy. The CEA software has been used to obtain specific heat at constant pressure C_p, molar mass $\mathcal{M}$, ratio of specific heats γ, dynamic viscosity μ, Prandtl number Pr in the throat section. Due to the frozen composition hypothesis, the flow properties have been kept constant over the whole domain. Using the perfect gas hypothesis, the internal energy can be expressed as

$$e(T,p)=C_vT \tag{10}$$

where C_v is the specific heat capacity at constant volume. Both C_p and C_v are considered independent of T, i.e. constant.

4.3. Numerical strategy

DbnsTurbFoam [59] is the adopted solver, belonging to a fork of OpenFOAM (Open Source Field Operation and Manipulation). It is a density-based transient solver designed for high speed compressible viscous flows, based on Finite Volume Method (FVM), therefore it is suitable to simulate the aerospike internal flow and its plume. It solves Equations (1)–(3) in the conservative form:

$$\frac{\partial\mathbf{U}}{\partial t}+\nabla\bullet\mathbf{F}-\nabla\bullet\mathbf{V}=\mathbf{R} \tag{11}$$

where $\mathbf{U}$ is the vector of conserved variable, $\mathbf{F}$ is the convective flux vector, $\mathbf{V}$ is the diffusive flux one and $\mathbf{R}$ is a source or forcing term.

$$\mathbf{U}=\begin{bmatrix}\rho\\ \rho\mathrm{u}\\ \rho e\end{bmatrix} \tag{12}$$

$$\mathbf{F}=\begin{bmatrix}\rho\mathrm{u}\\ \rho\mathrm{u}\otimes\mathrm{u}+p\mathbf{I}\\ \rho(\rho\xi+p)\mathrm{u}\end{bmatrix} \tag{13}$$

$$\mathbf{V}=\begin{bmatrix}0\\ \tau\\ \tau\bullet\mathrm{u}-\dot{\mathrm{q}}\end{bmatrix} \tag{14}$$

The flux $\mathbf{F}$ is evaluated on both sides of each mesh cell face directly from the state $\mathbf{U}$ using an approximate Riemann solver technique [60]. In particular in the following simulations, the HLLC scheme [60–62] has been used coupled with Barth-Jespersen limiter. This scheme has been chosen because it has been designed to solve the Riemann problem for the Euler equations [60]. Barth-Jespersen have designed a limiter on unstructured grids [63] that is able to guarantee stability with the drawback of reducing the accuracy.

The equations are integrated in time with an explicit, low-storage Runge-Kutta with four steps [64], in order to reduce the memory consumption, avoiding saving all intermediate solutions. The coefficients of the temporal scheme have been modified according to Ref. [65] to increase the stability region of the method. *dbnsTurbFoam* has been used with k-ω SST to model the turbulence: for k and ω equations, the BiConjugate Gradient Stabilized (BiCGStab) solver has been used with a simplified Diagonal-based Incomplete Lower-Upper (DILU) preconditioner to solve iteratively the linear system of equations. This method is a Krylov subspace method and has been adopted because has faster and smoother convergence than the BiConjugate Gradient (BiCG) solver [66].

The thermodynamics and transport flow properties have been calculated with the CEA software. The simulation meshes have been obtained using the open source software, *Gmsh* [67], dividing the simulation domain in regions and applying a different cell shape and size to each one. Where the flow direction is almost known a priori, a structured mesh has been used, while, in the opposite case, a triangular one has been chosen. The cell size has been tailored in order to have good accuracy close to the domain walls and to reduce the number of cell far away from them.

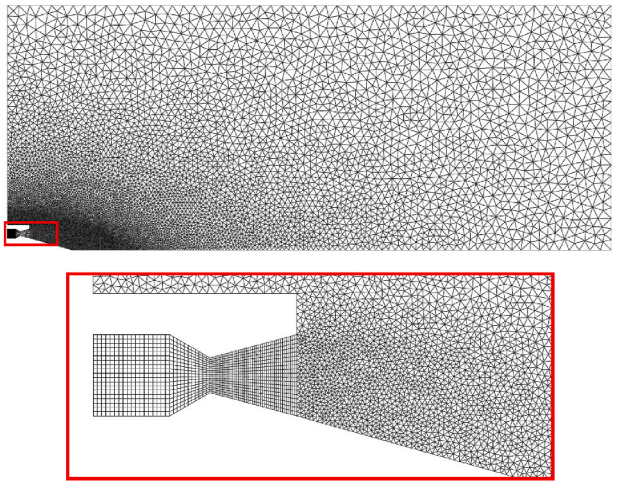

Fig. 11. Geometry mesh of the validation case: the mesh is coarser than the actual one for a better graphical representation. The red rectangle shows a magnification of the structured mesh region. (For interpretation of the references to color in this figure legend, the reader is referred to the Web version of this article.)

5. Validation of the numerical methodology

The numerical strategy has been validated with the experimental setup shown in Ref. [44] which reports a series of experiments performed on a linear plug nozzle tested varying the *NPR*: 3.1, 4.7 and 7.1. The test facility has a tank filled with compressed air that can reach a maximum pressure of about 10.34 bar. The linear plug has a width of 72 mm and it is held by a cantilever support system. Nine pressure sensors have been collocated in the plug central line, spaced by 10 mm. The total and ambient pressures are respectively measured about 250 mm and 10 mm upstream of the external cover end.

5.1. Simulation domain and mesh

Due to the wide plug region, it has been supposed that the experimental setup can be simulated through a 2D domain and by cause of the symmetric configuration, only the upper part of the geometry has been considered. The computational domain has been sized according to Ref. [21] in which the authors have performed simulations on the same geometry: the outlet and the farfields positions are described in Fig. 10. The outlet is located at 69 h_e from the throat section, the horizontal farfield is located at 25 h_e from the plug nozzle cowl, the inlet and the vertical farfield are positioned 1.4 h_e upstream of the throat section. In the aftermath, it is possible to check that the outlet is far away enough from the geometry in order to allow at the jet flow to reach the ambient pressure gradually and the horizontal farfield is far away enough to be not reached from the exiting jet flow.

Inside the convergent-divergent section, the flow direction is almost known, therefore this region can be discretized with a structured mesh with edges aligned to it. While outside, the flow has an unknown direction that changes with *NPR*, therefore this region has been discretized with an unstructured mesh. The mesh is finer close to the linear plug in order to capture the flow features: many oblique shock waves are located in the region over the plug, while it becomes coarser close to the outlet and the farfields. Fig. 11 shows the mesh elements density distribution: this mesh is not the actual one for graphic reasons. The red rectangle shows a magnification of the structured mesh region.

The used mesh has about 2×10^5 elements. The minimum, maximum and average edge length are respectively 2.98×10^{-2} mm, 14.7 mm and 1.2 mm.

The Co_{max} used in the following simulation is 0.1. Appendix B shows the thermodynamic and transport properties of the air used in the simulation of this geometry.

5.2. Initial transient

The total pressure at the inlet boundary rises linearly in time from ambient pressure 1×10^5 Pa up to each experimental test value in order to achieve the steady state condition. The time range considered for such pressure increase is $t \in [0, 0.02]$ s.

5.3. Boundary conditions

Boundary conditions are applied following the nomenclature described in Fig. 10.

5.3.1. Inlet

As previously described, total pressure varies linearly with time up to each experiment working condition. The inlet temperature T_{inlet} is equal to the ambient one (300K), independently of the air inlet pressure because the compressed air in the tank is in thermal equilibrium with the external environment. The velocity is free to adapt according to the pressure difference between the inlet and the first cell centre. ω and k have been calculated considering a developed flow inside the channel and isotropic turbulence [48]. The inlet values, for each experiment, are reported in Table 2.

5.3.2. Walls

For the pressure, the normal gradient to the wall has been imposed to zero, no slip condition for the velocity and adiabatic wall for the temperature. ω and k have been modelled using the wall functions [68] that allow to describe the behavior of these two variables close to the wall. The use of the wall functions allows to have a coarser grid resolution close to the wall: the first cell center near to the wall have to fall in the *log-layer region* or in closer region. Otherwise, these cells must be in the order of the *viscous sub layer*, which is very small. The wall functions used is shown in the OpenFOAM Guide [68]. A stepwise switch has been adopted between inertial sublayer and the viscous one.

5.3.3. Outlet, farfields

In these boundaries when the flow exits from the domain the ambient pressure 10^5 Pa is imposed, while when the flow enters into the domain, its total pressure is fixed to 10^5 Pa. The velocity adapts according to the pressure difference between the last cell center close to the outlet (or to the farfield) and the pressure imposed at the outlet (or at the farfields). For the temperature, ω and k when the flow exits from the domain a zero flux has been imposed on these three variables while when the flow enters inside the domain they are fixed to a given value, respectively $T_{o,f} = 300$ K [21], $\omega_{o,f} = 300\ s^{-1}$ and $k_{o,f} = 1.5 \times 10^{-10}\ m^2/s^2$.

Table 2
Boundary conditions values used in the validation simulations at different Nozzle Pressure Ratio *NPR*.

NPR [−]	p_{0inlet} [MPa]	T_{inlet} [K]	k_{inlet} [m^2/s^2]	ω_{inlet} [s^{-1}]	$k_{o,f}$ [m^2/s^2]	$\omega_{o,f}$ [s^{-1}]
3.1	0.31	300	12.30	2.14×10^4	1.50×10^{-10}	0.054
4.7	0.47	300	11.08	2.14×10^4	1.50×10^{-10}	0.054
7.1	0.71	300	10.00	2.14×10^4	1.50×10^{-10}	0.054

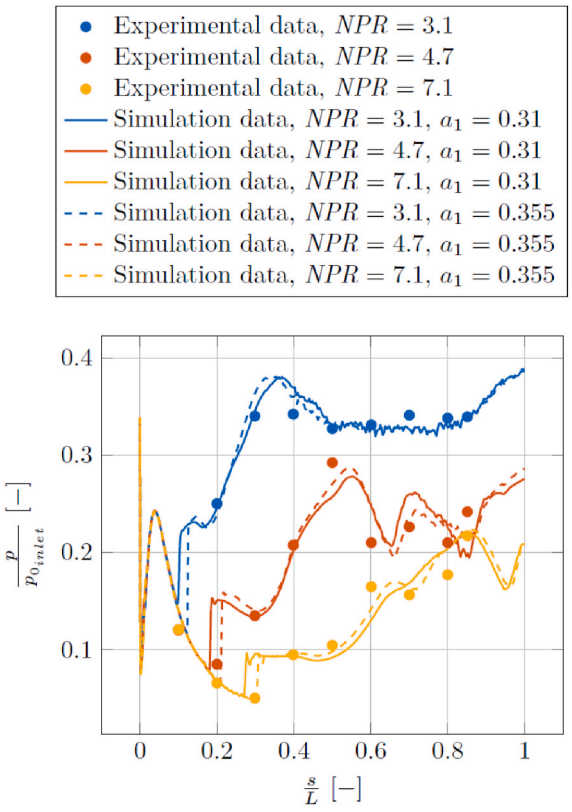

Fig. 12. Comparison between simulation results and experimental data: L is the plug length, s is a curvilinear coordinate along the plug, p is the static pressure and p_{0inlet} is the inlet total pressure.

Table 3
Pressure error with respect to experimental measurements at different Nozzle Pressure Ratio NPR.

NPR [−]	$e_{\text{dbnsTurbFoam},a_1=0.31}$ [−]	$e_{\text{dbnsTurbFoam},a_1=0.355}$ [−]
3.1	1.63×10^{-2}	1.37×10^{-2}
4.7	3.48×10^{-2}	2.09×10^{-2}
7.1	2.31×10^{-2}	1.44×10^{-2}

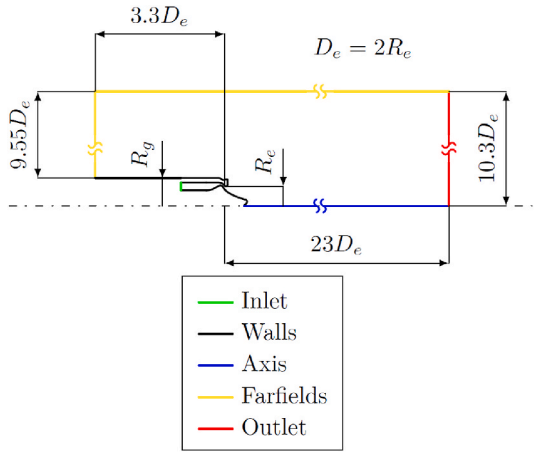

Fig. 13. Simulation domain and boundaries of DemoP1.

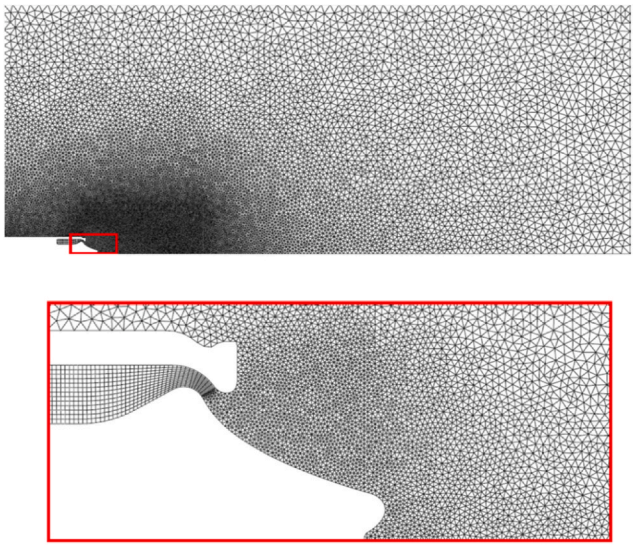

Fig. 14. DemoP1 mesh: the mesh is coarser than the used one in order to have a visible distribution of the mesh elements. The red rectangle shows a magnification of the mesh near the spike. (For interpretation of the references to color in this figure legend, the reader is referred to the Web version of this article.)

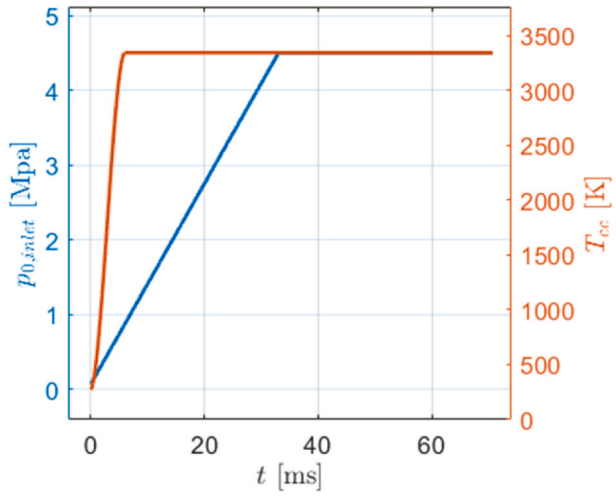

Fig. 15. Combustion chamber total pressure and temperature variation in time.

5.3.4. *Symmetric plane*

On the symmetry plane, for every variable, the partial derivative normal to the surface has been set to zero. Regarding the speed, the component normal to the surface has been imposed to zero.

Table 2 sums up the boundary conditions setting used at different *NPR*.

5.4. *Initial conditions*

The simulation starts with flow being still in every cell of the domain. The pressure and the temperature are uniform and equal to the ambient ones: respectively 10^5 Pa and 300 K. k and ω are treated analogously as described for the outlet and farfield boundary condition.

$$k_{init} = 1.5 \times 10^{-10}\ m^2/s^2 \tag{15}$$

$$\omega_{init} = 0.053\ s^{-1} \tag{16}$$

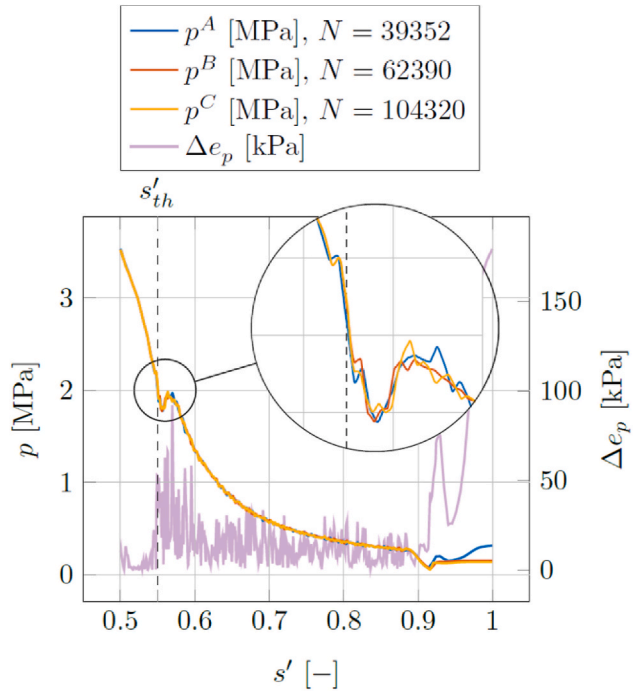

Fig. 16. Pressure distribution along DemoP1 internal wall, spike and base: N is the number of mesh cells, s' is a non-dimensional coordinate along the inner DemoP1 wall, 0 at inlet and 1 at the last aerospike base point on the symmetry axis. s'_{th} denotes the throat location.

Table 4
Evaluated thrusts in axial direction from mesh convergence analysis: the thrust error has been evaluated with respect to the finest mesh.

Mesh	N_{cells} [−]	T_{DemoP1} [N]	e_T [%]
A	39,532	1.884 × 104	0.39
B	62,390	1.875 × 104	−0.14
C	104,320	1.877 × 104	0.00

5.5. Validation results

The following results are extracted from the simulation at steady state conditions. Two groups of simulations have been run. In the first one, the k-ω SST parameters are the Menter's original ones, while in the second group the a_1 parameter has been changed from 0.31 to 0.355. According to Ref. [69], original k-ω SST model produces separation that are too large when the flow is considered compressible, therefore, this article suggests changing the a_1 coefficient from 0.31 to 0.355. Fig. 12 shows the validation results: the filled circles are the experimental results taken from Ref. [44], the solid line are the simulations results obtained imposing a1 = 0:31 while the dashed ones represent the results with $a_1 = 0.355$. According to Ref. [44] the error on pressure and total pressure measurements are respectively ±690 Pa and ±1379 Pa. The obtained solutions with $a_1 = 0.31$ are in a good agreement with the experimental results, but they anticipate the first oblique shock wave positions. The simulations characterized by $a_1 = 0.355$ instead are able to capture the flow separation in the right place improving the accuracy of the solutions, although the pressure sensors are placed too sparsely to obtain an accurate shock location. From the experimental data it can only be deduced that the shock is between the first and third pressure sensors.

Table 3 reports the non-dimensional errors obtained for every *NPR* and a_1 values. They have been calculated with the following formula

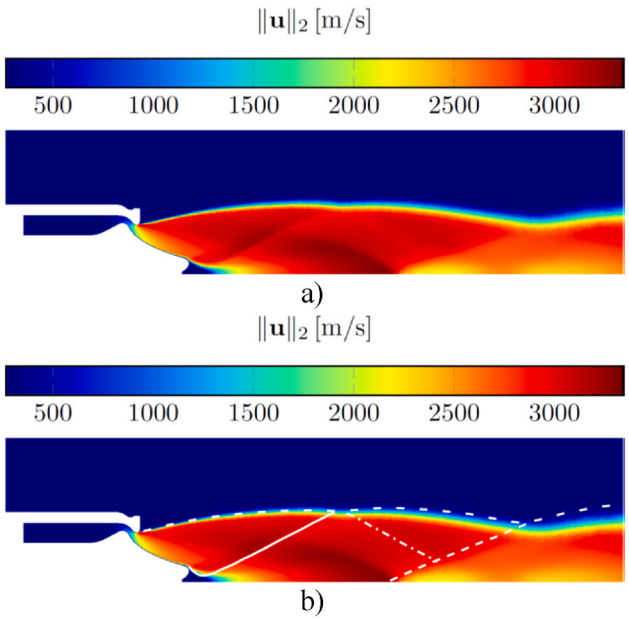

Fig. 17. Velocity field magnitude distribution obtained from the simulation a) with superimposed some reference lines b): trailing shock (solid line), trailing shock reflection (dash-dotted line), shear layer (loosely dashed line), shock wave (dashed line).

$$e = \sqrt{\sum_{j=1}^{n_{ps}} \left| \frac{p_j - p_j^{exp}}{p_{0_{inlet}}} \right|} \tag{17}$$

where p_j is the pressure obtained from the simulation at the j-th pressure sensor location, p_j^{exp} is the measured pressure by the j-th pressure sensors and n_{ps} is the number of pressure sensors: $n_{ps} = 9$.

Fig. 12 and Table 3 show that the simulation results are in good agreement with the experimental measurements, both in terms of absolute errors and trends. Based on these results, the solver has been considered validated and suitable for the simulation of the engine DemoP1.

6. Simulation of DemoP1

6.1. Simulation characteristics

6.1.1. Simulation domain and mesh

Due to high computational cost and the geometry symmetry, it has been decided to simulate only a 5° wedge of the actual geometry considering an axial symmetry.

Fig. 13 shows the simulated domain. The boundaries called farfields and outlet are positioned far away from the aerospike in order to avoid spurious results due to boundary conditions proximity. The computational domain has been sized according to Refs. [21,22,55], but, in order to reduce the computational cost, the outlet distance has been halved.

The used mesh has been designed in order to have a limited number of cells, about 62k, achieving a quite good solution but maintaining a low computational time (Fig. 14). The mesh is finer close to the aerospike, in order to capture the flow characteristics, while to keep low the total number of cells, the triangle edge size increases from 0.1 mm at the engine exit section up to 58 mm at the farfields and the outlet boundaries. An additional refinement region has been located in the plume close to the aerospike base in order to capture the shock reflections visible in the experimental results. Inside the combustion chamber, the flow direction is almost known because it is parallel to the walls, therefore a structured mesh has been used. Outside of the geometry, an

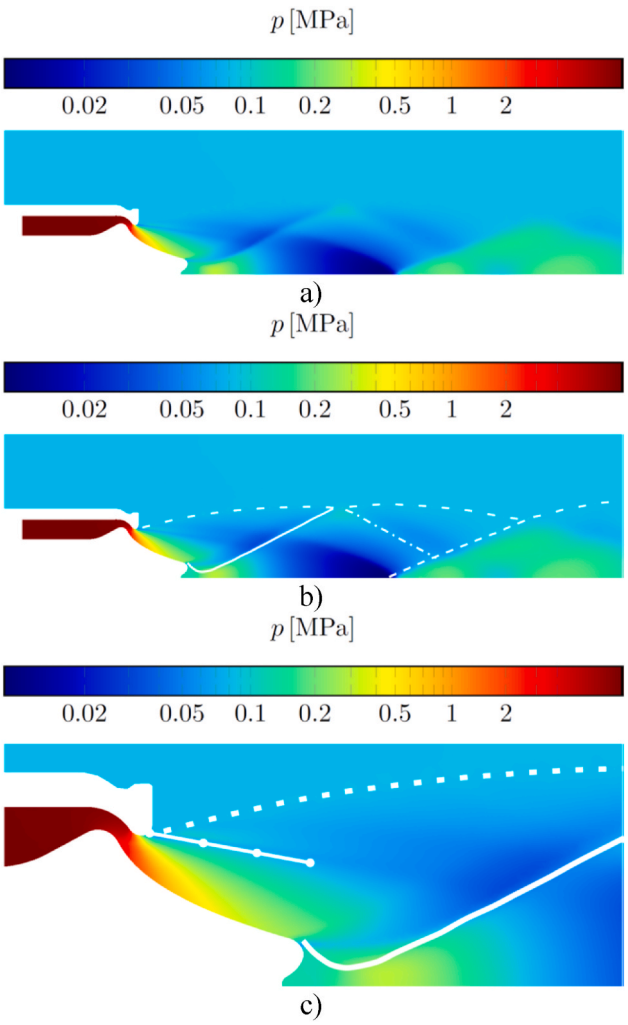

Fig. 18. Static pressure distribution obtained from the simulation: trailing shock (solid line), trailing shock reflection (dash-dotted line), shear layer (loosely dashed line), shock wave (dashed line), end of Prandtl-Meyer expansion (solid line with dots).

unstructured mesh has been adopted because of the unknown flow direction. Close to the divergent section, the mesh has been sized in order to capture the thin shear layer that starts from the wall and propagates toward right. In this region, too coarse mesh leads to thick shear layer and therefore the simulated flow would show a very smooth transition between the aerospike jet and outside air.

For these simulations, $Co_{max} = 0.08$ has been imposed because rising it too much would lead to too diffusive flow in the plume. Except in the initial transient, the maximum Δt used in these simulations is between 1×10^{-9} s to 1×10^{-8} s in order to satisfy the Courant number condition.

In these simulations, due to the high pressure ratio and the DemoP1 exit section aspect ratio, the flow will not separate on the spike. Only at the base, the flow will separate for geometrical reason, therefore a_1 has been set to 0.31.

The thermodynamic and transport properties of the exhaust gas have been calculated using the CEA (Appendix C).

6.1.2. Initial transient

The total pressure at the inlet boundary, corresponding to the combustion chamber, rises linearly in time from ambient pressure 101,325 Pa up to test value 4.05 MPa (40.5 bar) in order to achieve the steady state condition. The time range considered for such pressure increase is $t \in [0; 0.033]$ s. Differently from the validation simulations, the inlet

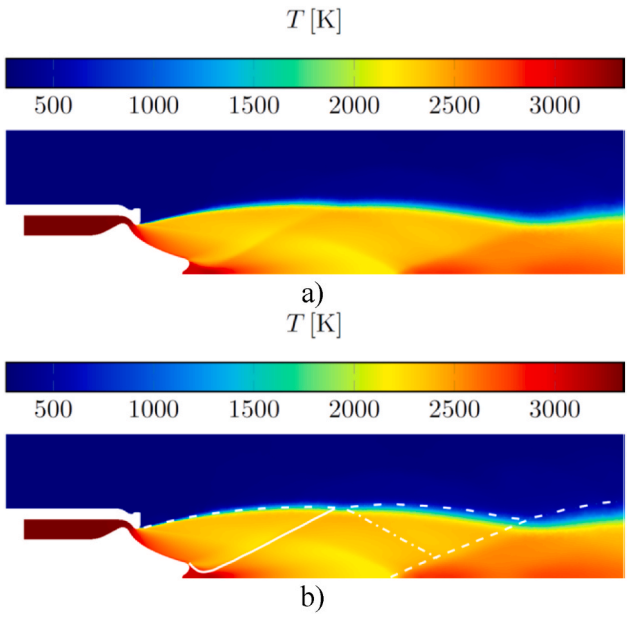

Fig. 19. Static temperature distribution obtained from the simulation a) with superimposed some reference lines b): trailing shock (solid line), trailing shock reflection (dash-dotted line), shear layer (loosely dashed line), shock wave (dashed line).

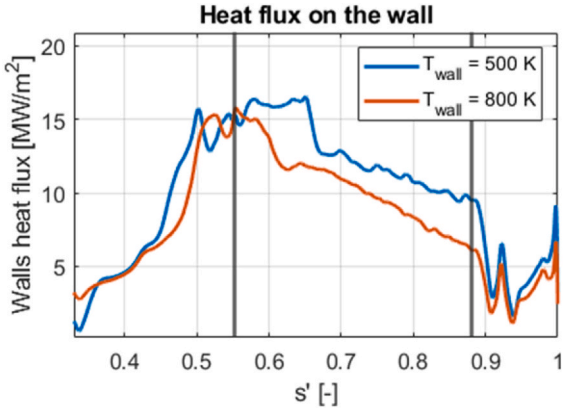

Fig. 20. Walls heat flux over the combustion chamber, lower internal wall, the spike and the base.

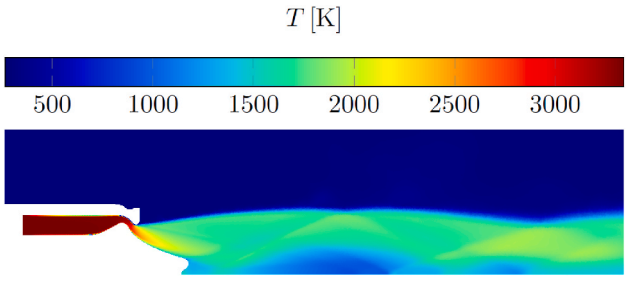

Fig. 21. Temperature distribution in fixed wall temperature simulation: Twall = 500K

temperature varies from the ambient temperature 300 K up to 3340 K, which is the estimated temperature within the combustion chamber (Appendix C), in 6.7 ms. Fig. 15 shows the inlet total pressure and static temperature variation in time.

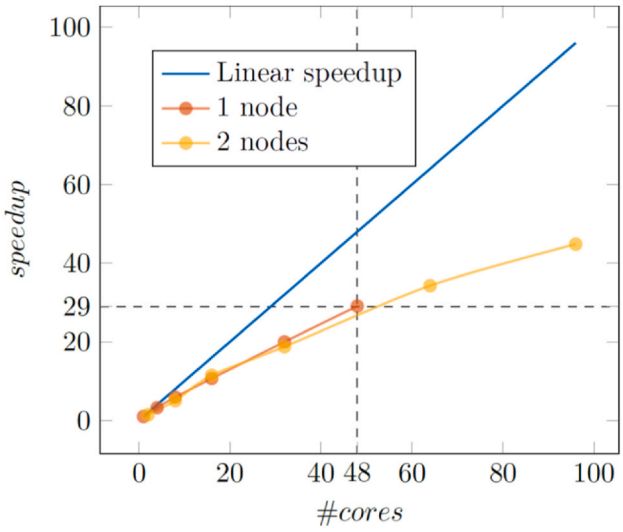

Fig. 22. Simulation speedup on GALILEO 100.

Table 5
Air thermodynamic properties obtained by CEA at ambient condition: $p_{amb} = 1 \times 10^5$ Pa and $T_{amb} = 300$ K.

Thermodynamics properties	
p_{amb}	1×10^5 Pa
T_{amb}	300 K
$C_{p_{amb}}$	1004.8 J/(kg K)
γ_{amb}	1.400
ρ_{amb}	1.161 kg/m^3
$\mathscr{M}_{amb}$	28.965 g/mol
$c_{s_{amb}}$	347.2 m/s

Table 6
Thermodynamic flow properties.

Thermodynamics properties	
p_{th}	2.552×10^6 Pa
T_{th}	3140 K
$C_{p_{th}}$	4651 J/(kg K)
γ_{th}	1.099
$\mathscr{M}_{th}$	19.84 g/mol
ρ_{inlet}	3.1089 kg/m^3
$c_{s_{inlet}}$	1272 m/s

Table 7
Transport flow properties.

Transport properties	
μ_{th}	1 × 10-4 kg/(m s)
PR_{th}	0.487
μ_{inlet}	1 × 10-4 kg/(m s)

6.1.3. Boundary conditions

Boundary conditions are applied following the nomenclature described in Fig. 13. The adopted boundary conditions are similar to the ones used in the validation simulations. Consequently, only the different one will be reported in the following paragraphs.

6.1.3.1. Inlet. As previously described, total pressure varies linearly with time up to the test working condition while the temperature rises following a fourth-order polynomial. The velocity adapts according to the pressure difference between the inlet and the first cell center close to this boundary. ω_{inlet} and k_{inlet} have been set respectively at 2.261×10^4 s^{-1} and 59.16 m^2/s^2.

6.1.3.2. Walls. For the pressure, the normal gradient to the wall has been imposed to zero, no slip condition for the velocity and adiabatic wall for the temperature. ω and k have been modelled using the wall functions [68] that allow to describe the behavior of these two variables close to the wall. A stepwise switch has been adopted between inertial sublayer and the viscous one.

6.1.3.3. Outlet, farfields. When the flow enters inside the domain the temperature is fixed to the ambient one (300 K), while when the flow exits form the domain the heat flux is set to zero. On these boundaries the total pressure, equal to 101,325 Pa, has been imposed when the flow enters inside the domain, while when it exits a zero flux condition has been used. $\omega_{o,f}$ and $k_{o,f}$ have been set respectively at 0.0125 s^{-1} and 1.5×10^{-10} m^2/s^2.

6.1.4. Initial conditions

The same initial conditions, shown in Section 5 for the validation case, have been employed in the simulation of DemoP1. For k and ω, the same value used for the outlet and farfields boundary conditions have been used.

6.1.5. Mesh convergence analysis

A mesh convergence analysis has been performed to check the dependency of the results from the mesh cell size. Three meshes, with an increasing number of elements, have been used: the coarsest one (A) has 39k cells, the medium one (B) has 62k cells and the finest one (C) has 104k. The finer meshes have been obtained refining the coarsest one in the region close to the spike and in the plume close to the engine. Near the outlet and the farfields, the mesh is kept almost the same in the three generated mesh. Fig. 16 shows the pressure distribution along the aerospike inner wall, the spike and the base, obtained with the used meshes. The violet line is the uncertainty on the pressure distribution, and it has been evaluated as follows:

$$\Delta e_p(s') = \max_{j\in[A,B,C]} p^j(s') - \min_{j\in[A,B,C]} p^j(s') \tag{18}$$

p^j is the pressure distribution obtained with the mesh j. Before the throat section the pressure distributions are almost identical, while they start to differ along the spike ($s'_{th} < s' \leq 0.9$) reaching a maximum uncertainty of 9.2×10^4 Pa. While along the base ($0.9 < s' \leq 1$), the pressure uncertainty rises up to 1.77×10^5 Pa due to the pressure distribution obtained with the mesh A, the coarsest one. The three lines are almost overlapped along the spike leading to an independence of the pressure solution at walls. Only the coarser mesh outputs a different pressure distribution at the aerospike base. Therefore, the mesh B is the right compromise between solution accuracy and calculation effort. The finest mesh C does not give a significant variation in the pressure distribution, but it requires a higher computational cost.

Table 4 shows the evaluated thrusts in axial direction for the three simulations. The obtained thrusts are very similar because the three obtained pressure distributions shown in Fig. 16 are almost identical: the mesh A predicts a little higher thrust due to the wrong pressure distribution at the base.

As an additional verification of the validity of the result, an accumulation error analysis has been done according to the methodology shown in Ref. [70]. The accumulation error has been estimated using the smallest time interval used in the simulation and its values in percentages is 4.22 %, inside the validity range of 5 % defined in the study, further validating the acceptability of the obtained results.

6.2. Simulation results

6.2.1. DemoP1 validation

The simulation with the mesh B has been chosen to be compared with the experimental results. Since the recorded video, described in Section 2, has been averaged in time also the simulation results will be averaged

before the comparison. The simulation outputs have been saved every 1 ms and the results have been averaged between 38 ms $\leq t \leq$ 45 ms.

Fig. 17a shows the velocity magnitude distribution obtained by the simulation. In this figure, the trailing shock and the shear layer are clearly seen. Close to the base there is a recirculation region because the flow is not able to remain attached to the aerospike wall. Fig. 17b displays the same content of Fig. 17a, overlayed with the flow features extracted from the experimental averaged results, as shown in Fig. 9. The solver has been capable to predict the trailing shock (solid white line in Fig. 17b), its reflection on the shear layer (dash-dotted white line in Fig. 17b), the shear layer (loosely dashed white line in Fig. 17b) and the shock which delimits a high temperature region (dashed white line in Fig. 17b).

Fig. 18a shows the pressure distribution near the aerospike in logarithmic color scale. Close to the throat, it is visible the Prandtl-Meyer expansion which ends beyond the spike base because the ambient pressure (101,325 Pa) is lower than the optimal one for which DemoP1 has been created (Section 2). Also in Fig. 18b, the overlayed white lines are the traces of the shock and expansion waves extracted from the experimental averaged results of Fig. 9. Fig. 18c highlights the second Prandtl-Meyer expansion fan at the end of the spike due to the spike truncation, which is immediately followed by the trailing shock which deviates the flow faraway from the axis. Also in this case the agreement with the with line extracted from the experiments is good.

Fig. 19 shows the temperature distribution in the simulated domain, and the superposition of the lines extracted from the experiments (white lines in Fig. 19b). Due to the hypothesis of adiabatic wall, the temperature does not decrease close to engine due to the cooling system.

The thrust obtained, integrating the static pressure distribution and the tangential stress over the wall surface, is 18.77 kN. This calculated value is obtained based on the hypothesis made for simulation model and therefore does not take into account efficiency of combustion, even though it is a good source of interesting evaluations such that the mass flow rate exiting the throat section and the corresponding discharge coefficient, respectively equal to 6.92 kg/s and 0.982.

6.2.2. *Heat flux evaluation*

A second set of simulations has been run imposing a fixed temperature value on the engine wall in order to estimate the wall heat flux. The mesh, the initial and the boundary conditions are the same ones used in the previous simulation described in this Section. The only difference is the boundary condition for the temperature which becomes a Dirichlet one. Two values of wall temperature have been used, 500 K and 800 K. Fig. 20 shows the walls heat flux distribution along the internal wall that starts at the end of the combustion chamber and ends with the spike and the base. It has been evaluated using Equation (14).

$$\dot{q} = \frac{C_p \mu}{Pr} \frac{\partial T}{\partial n} \tag{19}$$

The temperature of the flow at the inlet has been fixed at 3340 K while the one on the wall has been set to 500 K or 800K. The highest heat flux is close to the throat section (s' = 0.55). At the base the heat flux seems to be less dependent from the wall temperature. These results are consistent with the one used for DemoP1 design and allow to further validate the design process.

The temperature distribution shown in Fig. 21 is quite different from the previous result shown in Fig. 19, especially in the base region where the temperature is dropped from 2900K to about 1300K, while the performance estimation remains unchanged (0.2 % of difference of the estimated thrust with respect to the adiabatic walls simulation). This demonstrates that the heat loss through the wall is relevant for designing the cooling system but is almost negligible form the performance point of view, as demonstrated by the thrust evaluation.

7. Conclusions

DemoP1 shows that it is possible to economically produce aerospike with complex internal cooling system using the additive manufacturing technique. The Direct Metal Laser Sintering (DMLS), in combination with Multi-Volume Laser Energy Density (M-VLED), allows to build a complex cooling pipe system tailoring the material properties. The internal pipe surface roughness increases the heat convection with the cooling fluid, allowing a better cooling of the aerospike. The engine tests have confirmed the good mechanical and thermal capability of the copper alloy GRCop-42, developed by NASA, the structural integrity after long test and the effectiveness of the designed cooling system to maintain an acceptable temperature of the aerospike walls.

The numerical strategy, shown in Section 3.3, has been set up to simulate an aerospike. It has been successfully validated against data taken from literature, being able to predict the pressure distribution along the plug at different Nozzle Pressure Ratio (*NPR*) achieving a low average error. Then this methodology has been applied to DemoP1, and it has been capable to predict the shock lines like the trailing shock, the diamond shock and the shear layer seen in the DemoP1 experimental test (Fig. 17b, 18b and 19b). Finally, the solver has been used to estimate the thrust level of DemoP1 at sea-level condition, and to estimate the heat flux through the wall and then optimize the cooling system. The results obtained in terms of thrust for these last simulations allows to confirm that heat loss through the wall is relevant for designing the cooling system, but it is almost negligible form the performance point of view. The solver will serve in the future as a validated tool to investigate the behavior of the demonstrator at different NPR or at lower inlet temperatures, thus simulating non-optimal combustion efficiencies.

Declaration of competing interest

The authors declare that they have no known competing financial interests or personal relationships that could have appeared to influence the work reported in this paper.

Acknowledgment

We acknowledge the CINECA award under the ISCRA initiative, for the availability of high performance computing resources and support. We thank Pangea Aerospace for providing us the data concerning the manufacturing process of DemoP1 and the experimental data collected during the tests.

Appendix A. Benchmark of solver scalability

The simulations, that are performed in this work, require very small cells close to the geometry in order to capture the possible shock waves and to well solve the boundary layer satisfying the wall function constraint. Due to the small cells size and the high velocity reached by the flow, to keep a limited Courant number below a fixed threshold a very small Δt is required, which is usually in the order of 1×10^{-7} s to 1×10^{-9} s. Therefore, to obtain results in an acceptable time, the following simulations require an HPC facility. For these tasks GALILEO 100 [71] has been used. It is one of the clusters of the non-profit Consortium CINECA. It is composed by 528 computing nodes with 48 cores each. To determine which combination of nodes and cores allows to obtain the best performance, an analysis has been done on a simple simulation that has a mesh with 60k cells, comparable with the one that has been used to simulate the full engine behavior. Fig. 22 shows the speedup of the simulation increasing the number of core used. It is possible to notice that close to 48 cores the curve begins to flatten out, therefore to get results in acceptable time, it has been decided to run the simulations with 48 cores (1 nodes). The most expensive simulation required about 8 days.

Appendix B. Ambient conditions

The CEA software has been run to obtain the air thermodynamic and transport properties at 1 bar and 300K. They are shown in Table 5.

Appendix C. Thermodynamic and transport flow properties

For what concerns the thermodynamic and transport properties, the CEA software has been run in order to obtain the values related to the throat section since before it the flow is slow the chemical reaction could be fast enough to shift the chemical equilibrium according to local pressure and temperature, while after the throat section the flow speed increases too much and the chemical reactions have no time to reach a chemical equilibrium during the expansion phase close to the engine. The obtained thermodynamic and transport properties are shown in Tables 6 and 7. CEA outputs also the combustion chamber temperature: $T_{cc} = 3340$ K.

References

[1] N. Goncharov, V. Orlov, V. Rachuk, A. Shostak, R. Starke, Reusable launch vehicle propulsion based on the RD-0120 engine, in: 31st Joint Propulsion Conference and Exhibit, American Institute of Aeronautics and Astronautics, Reston, Virigina, 1995, https://doi.org/10.2514/6.1995-3003.

[2] F.B. Cowles, C.R. Foster, Experimental Study of Gas-Flow Separation in Overexpanded Exhaust Nozzles for Rocket Motors, 1949.

[3] G. Angelino, Approximate method for plug nozzle design, AIAA J. 2 (1964) 1834–1835, https://doi.org/10.2514/3.2682.

[4] J.F. Connors, R.W. Cubbison, G.A. Mitchell, Annular Internal-External-Expansion Rocket Nozzles for Large Booster Applications, Lewis Research Center, Cleveland, Ohio, 1961.

[5] G.V.R. Rao, Spike nozzle contour for optimum thrust, Planet. Space Sci. 4 (1961) 92–101, https://doi.org/10.1016/0032-0633(61)90125-8.

[6] G.P. Sutton, O. Biblarz, Rocket Propulsion Elements, ninth ed., John Wiley & Sons, 2016.

[7] P. Hill, C. Peterson, Mechanics and Thermodynamics of Propulsion, Pearson, 1991.

[8] G. Hagemann, H. Immich, T. Van Nguyen, G.E. Dumnov, Advanced rocket nozzles, J. Propul. Power 14 (1998) 620–634, https://doi.org/10.2514/2.5354.

[9] P.P. Nair, A. Suryan, H.D. Kim, Computational study of performance characteristics for truncated conical aerospike nozzles, J. Therm. Sci. 26 (2017) 483–489, https://doi.org/10.1007/s11630-017-0965-0.

[10] C.-H. Wang, Y. Liu, L.-Z. Qin, Aerospike nozzle contour design and its performance validation, Acta Astronaut. 64 (2009) 1264–1275, https://doi.org/10.1016/j.actaastro.2008.01.045.

[11] Ram3D. Aerospike. https://www.ram3d.co.nz/designing-an-aerospike-rocket-engine/, 2023. (Accessed 26 April 2023).

[12] Pangea Aerospace. https://pangeaaerospace.com/, 2023. (Accessed 26 April 2023).

[13] C.-H. Wang, Y. Liu, L.-Z. Qin, Aerospike nozzle contour design and its performance validation, Acta Astronaut. 64 (2009) 1264–1275, https://doi.org/10.1016/j.actaastro.2008.01.045.

[14] J. Sieder-Katzmann, M. Propst, M. Tajmar, C. Bach, Cold gas experiments on linear, thrust-vectored aerospike nozzles through secondary injection, in: Proceedings of the International Astronautical Congress, IAC, 2019.

[15] E. Schwarzer-Fischer, J. Abel, J. Sieder-Katzmann, M. Propst, C. Bach, U. Scheithauer, A. Michaelis, Study on CerAMfacturing of novel alumina aerospike nozzles by lithography-based ceramic vat photopolymerization, CerAM VPP), Materials 15 (2022) 3279, https://doi.org/10.3390/ma15093279.

[16] D.-S. Ha, H.J. Kim, Dynamic characteristic modeling and simulation of an aerospike-shaped pintle nozzle for variable thrust of a solid rocket motor, Acta Astronaut. 201 (2022) 364–375, https://doi.org/10.1016/j.actaastro.2022.09.031.

[17] Next Aero. https://nextaero.com.au/, 2023. (Accessed 26 April 2023).

[18] L. Nickels, Inside out 3D printing, Met. Powder Rep. 73 (2018) 148–150, https://doi.org/10.1016/j.mprp.2018.03.050.

[19] Flight of the aerospike, metal powder report 76 (2021) 12–15, https://doi.org/10.1016/S0026-0657(21)00296-4.

[20] Aenium Engineering - High Performance Additive Manufacturing, 2023. https://www.aenium.es/. (Accessed 31 January 2023).

[21] S. Soman, A. Suryan, P.P. Nair, H. Dong Kim, Numerical analysis of flowfield in linear plug nozzle with base bleed, J. Spacecraft Rockets 58 (2021) 1786–1798, https://doi.org/10.2514/1.A34992.

[22] P.P. Nair, A. Suryan, H.D. Kim, Computational study on flow through truncated conical plug nozzle with base bleed, Propulsion and Power Research 8 (2019) 108–120, https://doi.org/10.1016/j.jppr.2019.02.001.

[23] X.-Y. Liu, M. Cheng, Y.-Z. Zhang, J.-P. Wang, Design and optimization of aerospike nozzle for rotating detonation engine, Aero. Sci. Technol. 120 (2022) 107300, https://doi.org/10.1016/j.ast.2021.107300.

[24] J.Z. Ma, W. Bao, J. Wang, Experimental research of the performance and pressure gain in continuous detonation engines with aerospike nozzles, Aero. Sci. Technol. 140 (2023) 108464, https://doi.org/10.1016/j.ast.2023.108464.

[25] A.G. Kushnirenko, L.I. Stamov, V.V. Tyurenkova, M.N. Smirnova, E. V. Mikhalchenko, Three-dimensional numerical modeling of a rocket engine with solid fuel, Acta Astronaut. 181 (2021) 544–551, https://doi.org/10.1016/j.actaastro.2021.01.028.

[26] V.B. Betelin, A.G. Kushnirenko, N.N. Smirnov, V.F. Nikitin, V.V. Tyurenkova, L. I. Stamov, Numerical investigations of hybrid rocket engines, Acta Astronaut. 144 (2018) 363–370, https://doi.org/10.1016/j.actaastro.2018.01.009.

[27] V.V. Tyurenkova, L.I. Stamov, Flame propagation in weightlessness above the burning surface of material, Acta Astronaut. 159 (2019) 342–348, https://doi.org/10.1016/j.actaastro.2019.03.053.

[28] Eos M 290 (2023). https://www.eos.info/en/industrial-3d-printer/metal/eos-m-290.

[29] M.M. Attallah, R. Jennings, X. Wang, L.N. Carter, Additive manufacturing of Ni-based superalloys: the outstanding issues, MRS Bull. 41 (2016) 758–764, https://doi.org/10.1557/mrs.2016.211.

[30] Y. Shi, C. Yan, Y. Zhou, J. Wu, Y. Wang, S. Yu, Y. Chen, Materials for four-dimensional printing, in: Materials for Additive Manufacturing, Elsevier, 2021, pp. 679–739, https://doi.org/10.1016/B978-0-12-819302-0.00008-0.

[31] K.G. Cooper, J.L. Lydon, M.D. LeCorre, Z.C. Jones, D.S. Scannapieco, D.L. Ellis, B. A. Lerch, J.L. Lydon, M.D. LeCorre, Z.C. Jones, D.S. Scannapieco, D.L. Ellis, B. A. Lerch. Three-Dimensional Printing GRCop-42, 2018. http://www.sti.nasa.gov. (Accessed 31 January 2023).

[32] P.R. Gradl, S.E. Greene, C. Protz, B. Bullard, J. Buzzell, C. Garcia, J. Wood, R. Osborne, J. Hulka, K.G. Cooper, Additive manufacturing of liquid rocket engine combustion devices: a summary of process developments and hot-fire testing results, in: 2018 Joint Propulsion Conference, American Institute of Aeronautics and Astronautics, Reston, Virginia, 2018, https://doi.org/10.2514/6.2018-4625.

[33] P.R. Gradl, C.S. Protz, K. Cooper, D. Ellis, L.J. Evans, C. Garcia, GRCop-42 development and hot-fire testing using additive manufacturing powder bed fusion for channel-cooled combustion chambers, in: AIAA Propulsion and Energy 2019 Forum, American Institute of Aeronautics and Astronautics, Reston, Virginia, 2019, https://doi.org/10.2514/6.2019-4228.

[34] M.St Weglowski, S. Błacha, A. Phillips, Electron beam welding—techniques and trends, in: Welding and Joining of Aerospace Materials, Elsevier, 2012, pp. 157–198, https://doi.org/10.1016/B978-0-12-819140-8.00006-7.

[35] Omniseal Solution, Omniseal Polymers: Spring Energized Seals, 2021. https://www.omniseal-solutions.com/sites/hps-mac3-seals-seals/files/2022-09/Omniseal-Spring-Energized-Seal-Handbook-2022-EU.pdf. (Accessed 31 January 2023).

[36] W. Koschel, P8?The new French/German test facility for H2/O2 high pressure rocket engine combustion research, Int. J. Hydrogen Energy 23 (1998) 683–694, https://doi.org/10.1016/S0360-3199(97)00088-8.

[37] A. Haberzettl, D. Gundel, K. Bahlmann, J. Thomas, J. Kretschmer, P. Vuillermoz, European research and technology test bench P8 for high pressure liquid rocket propellants, in: 36th AIAA/ASME/SAE/ASEE Joint Propulsion Conference and Exhibit, American Institute of Aeronautics and Astronautics, Reston, Virigina, 2000, https://doi.org/10.2514/6.2000-3307.

[38] Photron Photron, Mini UX100 Datasheet, 2021. https://photron.com/wp-content/uploads/2021/08/Mini-UX-2021.pdf. (Accessed 26 April 2023).

[39] Pressure Transmitter for General Industrial Applications, Model A-10. Datasheet, 2021. https://www.wika.com/media/Data-sheets/Pressure/Pressure-sensors/ds_pe8160_en_co.pdf. (Accessed 26 April 2023).

[40] T.B. Gatski, J.-P. Bonnet, Compressible turbulent flow, in: Compressibility, Turbulence and High Speed Flow, Elsevier, 2013, pp. 39–77, https://doi.org/10.1016/B978-0-12-397027-5.00003-4.

[41] OpenFOAM Foam-Extend Toolbox, 2023. https://sourceforge.net/projects/foam-extend/.

[42] E.F. Toro, The HLLC Riemann solver, Shock Waves 29 (2019) 1065–1082, https://doi.org/10.1007/s00193-019-00912-4.

[43] CEA Software, 2023. (n.d.), https://software.nasa.gov/software/LEW-17687-1. (Accessed 26 April 2023).

[44] K. Chutkey, M. Viji, S.B. Verma, Effect of clustering on linear plug nozzle flow field for overexpanded internal jet, Shock Waves 27 (2017) 623–633, https://doi.org/10.1007/s00193-017-0707-y.

[45] Y. Huang, P. Wang, Y. Dou, F. Xing, Chemical non-equilibrium flow analysis of H2 fueled scramjet nozzle, Case Stud. Therm. Eng. 5 (2015) 89–97, https://doi.org/10.1016/j.csite.2015.02.002.

[46] G. Buresti, A note on Stokes' hypothesis, Acta Mech. 226 (2015) 3555–3559, https://doi.org/10.1007/s00707-015-1380-9.

[47] G. Buresti, Elements of Fluid Dynamics, IMPERIAL COLLEGE PRESS, 2012, https://doi.org/10.1142/p848.

[48] F.R. Menter, Two-equation eddy-viscosity turbulence models for engineering applications, AIAA J. 32 (1994) 1598–1605, https://doi.org/10.2514/3.12149.

[49] B.E. Launder, D.B. Spalding, The numerical computation of turbulent flows, Comput. Methods Appl. Mech. Eng. 3 (1974) 269–289, https://doi.org/10.1016/0045-7825(74)90029-2.

[50] D.C. Wilcox, Reassessment of the scale-determining equation for advanced turbulence models, AIAA J. 26 (1988) 1299–1310, https://doi.org/10.2514/3.10041.

[51] D. Wilcox, Multiscale model for turbulent flows, in: 24th Aerospace Sciences Meeting, American Institute of Aeronautics and Astronautics, Reston, Virigina, 1986, https://doi.org/10.2514/6.1986-29.

[52] D. Wilcox, Turbulence Modeling for CFD, third ed., Hardcover), 2006.

[53] D.C. Wilcox, Formulation of the k-w turbulence model revisited, AIAA J. 46 (2008) 2823–2838, https://doi.org/10.2514/1.36541.

[54] A. Naghib-Lahouti, M. Nazarinia, E. Tolouei, Design and numerical analysis of aerospike nozzles with different plug shapes to compare their performance with a

conventional nozzle, in: AIAC-11 Eleventh Australian International Aerospace Congress, 2004.
[55] B. Zang, V. U S, T.H.D. New, OpenFOAM based numerical simulation study of an underexpanded supersonic jet, in: 55th AIAA Aerospace Sciences Meeting, American Institute of Aeronautics and Astronautics, Reston, Virginia, 2017, https://doi.org/10.2514/6.2017-0747.
[56] F.R. Menter, M. Kuntz, R. Langtry, Ten years of industrial experience with the SST turbulence model turbulence heat and mass transfer, Cfd.Spbstu.Ru. 4 (2003).
[57] S. Gordon, B.J. Mcbride. Computer program for calculation of complex chemical equilibrium compositions and applications, Analysis, 1994, p. 1311. Part 1.
[58] B.J. McBride, S. Gordon, Computer Program for Calculation of Complex Chemical Equilibrium Compositions and Applications: II. Users Manual and Program Description, NASA Reference Publication, 1996, p. 1311.
[59] Solvers | CFD with A MISSION, 2023. https://caefn.com/openfoam/solvers.
[60] E.F. Toro, Riemann Solvers and Numerical Methods for Fluid Dynamics, Springer Berlin Heidelberg, Berlin, Heidelberg, 2009, https://doi.org/10.1007/b79761.
[61] E.F. Toro, M. Spruce, W. Speares, Restoration of the contact surface in the HLL-Riemann solver, Shock Waves 4 (1994) 25–34, https://doi.org/10.1007/BF01414629.
[62] P. Batten, N. Clarke, C. Lambert, D.M. Causon, On the choice of wavespeeds for the HLLC Riemann solver, SIAM J. Sci. Comput. 18 (1997) 1553–1570, https://doi.org/10.1137/S1064827593260140.
[63] T. Barth, D. Jespersen, The design and application of upwind schemes on unstructured meshes, in: 27th Aerospace Sciences Meeting, American Institute of Aeronautics and Astronautics, Reston, Virigina, 1989, https://doi.org/10.2514/6.1989-366.
[64] A. Arnone, M.-S. Liou, L. Povinelli, Multigrid time-accurate integration of Navier-Stokes equations, in: 11th Computational Fluid Dynamics Conference, American Institute of Aeronautics and Astronautics, Reston, Virigina, 1993, https://doi.org/10.2514/6.1993-3361.
[65] M.-H. Lallemand, Dissipative Properties of Runge-Kutta Schemes with Upwind Spatial Approximation for the Euler Equations, INRIA, 1990. https://hal.inria.fr/inria-00075385. (Accessed 31 January 2023).
[66] H.A. van der Vorst, Bi-Cgstab, A fast and smoothly converging variant of Bi-cg for the solution of nonsymmetric linear systems, SIAM J. Sci. Stat. Comput. 13 (1992) 631–644, https://doi.org/10.1137/0913035.
[67] C. Geuzaine, J.-F. Remacle, Gmsh, A 3-D finite element mesh generator with built-in pre- and post-processing facilities, Int. J. Numer. Methods Eng. 79 (2009) 1309–1331, https://doi.org/10.1002/nme.2579.
[68] OpenFOAM, User Guide: omegaWallFunction, 2023. https://www.openfoam.com/documentation/guides/latest/doc/guide-bcs-wall-turbulence-omegaWallFunction.html. (Accessed 31 January 2023).
[69] N. Georgiadis, D. Yoder, Recalibration of the shear stress transport model to improve calculation of shock separated flows, in: 51st AIAA Aerospace Sciences Meeting Including the New Horizons Forum and Aerospace Exposition, American Institute of Aeronautics and Astronautics, Reston, Virigina, 2013, https://doi.org/10.2514/6.2013-685.
[70] N.N. Smirnov, V.B. Betelin, V.F. Nikitin, L.I. Stamov, D.I. Altoukhov, Accumulation of errors in numerical simulations of chemically reacting gas dynamics, Acta Astronaut. 117 (2015) 338–355, https://doi.org/10.1016/j.actaastro.2015.08.013.
[71] GALILEO100 | SCAI, 2023. https://www.hpc.cineca.it/hardware/galileo100. (Accessed 31 January 2023).